JOURNAL OF THERMOPHYSICS AND HEAT TRANSFER
Vol. 18, No. 4, October–December 2004

Thermally Developing Electroosmotic Convection in Rectangular Microchannels with Vanishing Debye-Layer Thickness

B. D. Iverson,* D. Maynes,† and B. W. Webb‡
Brigham Young University, Provo, Utah 84602

Thermally developing electroosmotically generated flow in rectangular ducts has been analyzed for the constant-wall-temperature boundary condition. In such flow, fluid motion is induced not by an applied pressure gradient, but by an applied electric potential. For fluid-tube-material combinations that yield a Debye layer of vanishing thickness, the velocity distribution is essentially uniform across the duct cross section. In addition, the applied potential gradient induces an electrical current that results in volumetric heating in the fluid. An analytical solution to the hydrodynamically developed, thermally developing transport for such a flow is presented in this paper. The effect of variations in the duct aspect ratio, the relative magnitude of the volumetric generation, and the Peclet number on the thermal transport are explored over the possible ranges of these parameters. The solution reveals a local minimum in the streamwise variation of the local perimeter-averaged Nusselt number for moderate, positive values of the dimensionless duct inlet fluid temperature. For negative inlet temperatures, the fluid is initially heated and then cooled, creating a singularity in the local, perimeter-averaged Nusselt number at this transition. Far downstream, heat transport approaches constant-wall-heat-flux conditions for both positive and negative inlet temperatures. The fully developed Nusselt number decreases from a maximum for the parallel-plate configuration to a minimum for the square duct. Electroosmotically generated flow exhibits considerably longer thermal-entry regions than pressure-driven flow, and the development length is observed to be a function of Peclet number, dimensionless inlet temperature, and channel aspect ratio.

Nomenclature

A	=	channel aspect ratio, b/a
a	=	channel width
b	=	channel height
C	=	fluid specific heat
D_h	=	hydraulic diameter
h	=	convective-heat-transfer coefficient
i_e	=	conduction-current density
k	=	fluid thermal conductivity
Nu	=	Nusselt number (hD_h/k)
Nu_{fd}	=	fully developed Nusselt number
Nu_{min}	=	minimum Nusselt number
Nu_η	=	local Nusselt number along horizontal channel wall
Nu_ζ	=	local Nusselt number along vertical channel wall
$\overline{Nu}_X$	=	local perimeter-averaged Nusselt number
P	=	channel perimeter
Pe	=	Peclet number (UD_h/α)
q''_w	=	wall heat flux
T	=	absolute temperature
T_e	=	channel-fluid-inlet temperature
T_m	=	mixed mean temperature
T_w	=	channel-wall temperature
u	=	local fluid velocity
V	=	applied streamwise electric potential
X	=	dimensionless streamwise coordinate, $x/D_h Pe$
X_{fd}	=	dimensionless thermal-development length, $x_{\text{fd}}/D_h Pe$
X_{min}	=	dimensionless axial location of minimum Nusselt number
x	=	streamwise coordinate
x_{fd}	=	thermal-development length
y	=	horizontal channel coordinate
Z	=	wall zeta potential
z	=	vertical channel coordinate
α	=	fluid thermal diffusivity
Γ	=	geometric parameter, $4/(1+A)^2$
ε	=	fluid dielectric constant
ζ	=	dimensionless vertical coordinate, z/b
η	=	dimensionless horizontal coordinate, y/a
θ	=	dimensionless temperature, $(T-T_w)/(i_e^2\sigma D_h^2/k)$
θ_e	=	dimensionless channel-inlet temperature, $(T_e-T_w)/(i_e^2\sigma D_h^2/k)$
θ_m	=	dimensionless fluid mixed mean temperature, $(T_m-T_w)/(i_e^2\sigma D_h^2/k)$
μ	=	absolute viscosity
μ_{eo}	=	electroosmotic mobility
ν	=	kinematic viscosity
ρ	=	fluid density
σ	=	fluid electrical resistivity
Φ	=	dimensionless local perimeter-averaged wall heat flux

Received 11 July 2003; revision received 29 April 2004; accepted for publication 1 June 2004.

*Graduate Student, Department of Mechanical Engineering, 435 CTB.
†Associate Professor, Department of Mechanical Engineering, 435 CTB. Member AIAA.
‡Professor, Department of Mechanical Engineering, 435 CTB. Member AIAA.

Introduction

ELECTROOSMOTICALLY generated flow differs significantly from classical pressure-driven flow, principally because the flow is driven by an applied voltage gradient instead of an applied pressure gradient. Electroosmosis was first reported nearly two centuries ago[1] and is now seeing significant use in microscale chemical-separation processes. Since it enables fluid pumping without generation of large pressures or manufacture of microscale pumping systems, electroosmotic pumping is a viable alternative to pressure-generated transport in microscale systems.[2–6] As microfluidic systems continue to mature, the use of electroosmosis as the primary driving mechanism is likely to increase. Electroosmosis provides much more accurate control at low volume-flow rates than pressure-driven flow.[7] Further, if the microchannel diameter is sufficiently large, the velocity profile will be uniform in shape, which is particularly important in many electrophoresis applications.[5] For other applications thermal transport will also be important, if not the desired result (e.g., microscale cooling or heating systems).

A rigorous treatise on the fundamentals of electroosmotic flow has been given elsewhere.[8] Therefore, only a brief summary of the phenomenon is given here. When in contact with a polar solution most solid surfaces will acquire a relative electric charge with respect to the bulk solution. For example, glass and fused silica capillaries carry dissociable silanol groups on the surface and are therefore negatively charged when in contact with polar liquids. The net effect on the fluid is the formation of a region adjacent to the solid surface called the electric double layer (EDL) where a distribution of excess charge exists, increasing from a neutral charge in the core fluid to a maximum at the solid–liquid interface. The thickness of this layer is characterized by the Debye length, which is defined to be the distance from the wall at which the net charge has decreased to $1/e$ (37%) of the surface charge. It is due to this nonuniform charge distribution that fluid motion is generated when an axially imposed voltage potential is applied. In the EDL the imposed voltage potential exerts a body force on the charged ions, acting in the direction of the tube axis. This force is a maximum at the wall but vanishes in the fluid core. Consequently, the fluid in the thin EDL will migrate in the direction of decreasing voltage potential and, due to viscous shear, will draw the bulk fluid along as well. For the scenario in which the solid surface acquires a positive charge, flow will be induced in the direction of increasing voltage potential. When the Debye length is much smaller than the duct radius, the resulting profile is nearly uniform in shape and is described by the Helmholtz–Smoluchowski equation[8]:

$$U = -\frac{\varepsilon Z}{\mu}\frac{\mathrm{d}V}{\mathrm{d}x} \tag{1}$$

Z is the so-called zeta potential, or the electric potential near the wall, and is determined by the charge-density distribution in the fluid.[8] The coefficients ε and μ are the fluid dielectric constant and viscosity, respectively, and $\mathrm{d}V/\mathrm{d}x$ is the potential gradient applied along the duct length. The combination $\varepsilon Z/\mu$ is often termed the electroosmotic mobility of the liquid, μ_{eo}. Only as the channel-radius-to-Debye-length ratio decreases will the velocity distribution depart from the uniform (plug-flow) behavior. However, with the very thin Debye layers characteristic of many electroosmotic flow applications, the channel-radius-to-Debye-length ratio is $O(100)$ or greater and is thus the scenario considered here. In reality, the fluid velocity does not slip at the wall, as the Helmholtz–Smoluchowski equation suggests, but transitions across the EDL from zero to its near-constant value in the core fluid. For example, the Debye length for water in a fused silica capillary is of order 0.1–1 μm [8]. Thus, for electroosmotically driven flow of water in a parallel-plate channel of spacing 200 μm, the velocity profile would be uniform over more than 99% of the channel cross section, and may thus be well approximated as plug flow. It is further noted that typical electroosmotic velocity magnitudes are very small—in the range 0.1–15 mm/s.[9]

In addition to exhibiting velocity distributions distinctly different from those of pressure-driven flow, electroosmotic flow also exhibits volumetric heating in the fluid. The combination of these two effects results in thermal transport quite different from classical pressure-driven laminar flow. The applied voltage potential induces an electrical current composed of the so-called conduction and convection components. The conduction current is accurately modeled using Ohm's law.[10] The convection current represents the net transport of charge due to bulk-fluid motion. For microtubes of large radius the conduction current is uniform across the duct cross section and, thus, the induced electrical Joule heating is uniform as well (provided the fluid resistivity, σ (Ωm), is constant).[11] Expressed on a per-unit-volume basis, the Joule heating is equal to $i_e^2\sigma$, where i_e is the conduction-current density (A/m^2). A second source of energy generation is that due to viscous heating. Viscous heating represents a spatially nonuniform source of energy that is dependent on the velocity profile and is of magnitude $\mu(\partial u/\partial y)^2$, where u is the streamwise velocity and y is the wall-normal coordinate. The total volumetric heating is the sum of Joule and viscous heating. Although significant velocity gradients arise in electroosmotic flow, prior work has shown that viscous dissipation exercises negligible influence on the fully developed thermal transport for vanishingly thin EDL and realistic magnitudes of the Joule heating.[12]

The hydrodynamic fundamentals of electroosmotic flow have been explored in the literature by multiple investigators, both analytically[10,11,13] and experimentally.[14–18] However, relatively little work has appeared characterizing the convective-heat-transfer behavior of electroosmotically generated flows. The electrokinetic effects on the frictional and heat-transfer characteristics for round and rectangular microchannels have been explored for pressure-driven flows.[19–21] The induced electrokinetic potential was found to result in a reduced flow rate, a greater friction factor, and a reduced Nusselt number in comparison to those of classical laminar pressure-driven flow. Others have characterized the effect of Joule heating on chemical-separation efficiency in capillary electrophoresis.[22–24] There also exists some related early work exploring the effect of volumetric heating (induced by nuclear reaction) on thermal development in circular channels under pressure-driven flow conditions.[25,26] Recently a study has reported on fully developed thermal transport in purely electroosmotically driven flow in circular and parallel-plate microchannels for a relevant range of duct-diameter-to-Debye-length ratios.[27] Both constant-wall-temperature and constant-wall-heat-flux boundary conditions were considered. The effects of superimposed pressure gradients on fully developed thermal transport in electroosmotically generated flow have also been characterized for both pressure-assisted and pressure-opposed scenarios.[28]

There appears to be no prior work that addresses the thermally developing convective-transport characteristics of purely electroosmotically generated flow in rectangular microchannels of varying aspect ratio. Because micromachined channels are often rectangular in cross section, the objective of the present work is the exploration of the thermally developing flow in a rectangular microchannel under constant-wall-temperature conditions for large duct-diameter-to-Debye-length ratio. In particular, the effects of varying microchannel aspect ratio and the magnitude of the volumetric heating are explored over the range of possible values.

Analysis

Consider steady, hydrodynamically developed, thermally developing electroosmotic flow in a rectangular microtube of height b and width a [hydraulic diameter $D_h = 2b/(1 + b/a)$]. The walls of the duct are maintained at constant temperature. Assuming steady-state thermal transport with constant thermophysical properties, and neglecting viscous dissipation, the differential energy equation may be written as

$$(\boldsymbol{u}\cdot\nabla)T = \alpha\nabla^2 T + i_e^2\sigma\big/\rho C \tag{2}$$

The last term in Eq. (2) represents the spatially uniform volumetric source of energy that causes Joule heating in the fluid.

For the case of vanishing Debye layer (large hydraulic diameter/Debye length ratio), the velocity profile may be approximated as uniform with magnitude U across the tube cross section. The velocity magnitude is dependent on the electroosmotic properties and the streamwise electrical-potential gradient in the fluid. For the coordinate system defined in Fig. 1, the nondimensional form of the

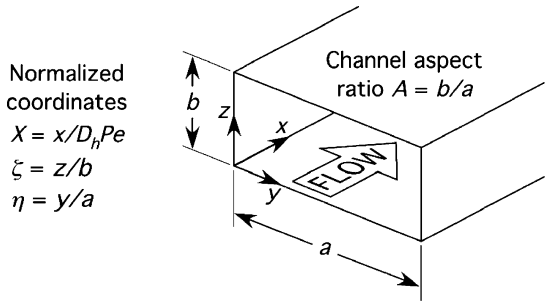

Fig. 1 Coordinate system and channel cross section schematic.

energy equation is

$$\frac{\partial\theta}{\partial X} = \frac{1}{Pe^2}\frac{\partial^2\theta}{\partial X^2} + \Gamma A^2\frac{\partial^2\theta}{\partial\eta^2} + \Gamma\frac{\partial^2\theta}{\partial\zeta^2} + 1 \tag{3}$$

where the dimensionless temperature has been defined as $\theta = (T - T_w)/(i_e^2\sigma D_h^2/k)$. The dimensionless streamwise coordinate conventionally used to characterize the thermal development in convection-dominated (high-Pe) flows is $X = x/D_h Pe$. Although the Peclet number for electroosmotic flow is $O(0.1\text{–}10)$, this dimensionless coordinate was adopted here to facilitate comparison with results for thermal development in classical pressure-driven flows. Thus, the dimensionless coordinates are $X = x/D_h Pe$, $\eta = y/a$, and $\zeta = z/b$. The channel aspect ratio is defined as $A = b/a$, and the geometric parameter Γ in Eq. (3) is $\Gamma = 4/(1+A)^2$. T_w is the constant tube-wall temperature, and the Peclet number is defined as $Pe = U D_h/\alpha$. Note that as the aspect ratio $A \to 0$, diffusion in the y-direction becomes negligible and the cross section approaches parallel-plate conditions.

The thermal inlet and boundary conditions are, respectively,

$$\theta(0, \eta, \zeta) = \theta_e \tag{4}$$

$$\theta(X, 0, \zeta) = 0 \tag{5a}$$

$$\theta(X, 1, \zeta) = 0 \tag{5b}$$

$$\theta(X, \eta, 0) = 0 \tag{5c}$$

$$\theta(X, \eta, 1) = 0 \tag{5d}$$

The dimensionless inlet temperature $\theta_e = (T_e - T_w)/(i_e^2\sigma D_h^2/k)$ reflects not only the fluid–wall temperature difference (and its sign) at the channel inlet, but also the strength of the volumetric heating in the fluid. For a given $T_e - T_w$, higher Joule heating results in a lower magnitude of θ_e. It is also important to note that the dimensionless inlet temperature θ_e may take on values both positive (for $T_e > T_w$) and negative (for $T_e < T_w$), with a range of magnitudes from 0 (e.g., for $|T_e - T_w| \to 0$ or infinitely high Joule heating) to ∞ (e.g., for vanishing Joule heating). Thus, the condition $\theta_e \to \infty$ corresponds to the classical case of plug-flow convection in a rectangular duct.[29]

Equation (3) is a linear, nonhomogeneous, partial differential equation that can be solved using one of several classical methods. The integral transform method was used here,[30] and the solution for the local fluid temperature with an imposed constant tube wall temperature is

$$\theta(X, \eta, \zeta) = 4\sum_{n=1}^{\infty}\sum_{m=1}^{\infty}\frac{(1-\cos\gamma_m)(1-\cos\lambda_n)}{\gamma_m\lambda_n}\left[\left(1 - \frac{1}{\beta_{n,m}}\right)\right.$$

$$\left.\times\, e^{\left(1-\sqrt{1+4\beta_{n,m}/Pe^2}\right)XPe^2/2} + \frac{1}{\beta_{n,m}}\right](\sin\gamma_m\eta)(\sin\lambda_n\zeta) \tag{6}$$

where

$$\beta_{n,m} = \theta_e\Gamma\left(A^2\gamma_m^2 + \lambda_n^2\right) \tag{7}$$

The eigenvalues γ_m and λ_m are found from the eigenconditions $\sin(\gamma_m) = 0$ and $\sin(\lambda_m) = 0$. The local fluid mixed mean temperature, $\theta_m = (T_m - T_w)/(i_e^2\sigma D_h^2/k)$, may be determined by integration of Eq. (6) over the duct cross section to be

$$\theta_m(X) = 4\sum_{n=1}^{\infty}\sum_{m=1}^{\infty}\frac{(1-\cos\gamma_m)^2(1-\cos\lambda_n)^2}{\gamma_m^2\lambda_n^2}$$

$$\times\left[\left(1 - \frac{1}{\beta_{n,m}}\right)e^{\left(1-\sqrt{1+4\beta_{n,m}/Pe^2}\right)XPe^2/2} + \frac{1}{\beta_{n,m}}\right] \tag{8}$$

The local, perimeter-averaged Nusselt number at a given streamwise location X is found by averaging the local wall heat flux over the duct perimeter P:

$$\overline{Nu}_X = \frac{1}{P}\int_P \frac{q_w'' D_h}{k(T_m - T_w)}\,\mathrm{d}P \tag{9}$$

Evaluation of this integral yields

$$\overline{Nu}_X = \frac{2}{\Delta}\sum_{n=1}^{\infty}\sum_{m=1}^{\infty}\frac{(1-\cos\gamma_m)(1-\cos\lambda_n)}{\gamma_m\lambda_n}$$

$$\times\left[\left(1 - \frac{1}{\beta_{n,m}}\right)e^{\left(1-\sqrt{1+4\beta_{n,m}/Pe^2}\right)XPe^2/2} + \frac{1}{\beta_{n,m}}\right]$$

$$\times\left[\frac{1}{(1+1/A)^2}\left(\frac{\gamma_m}{\lambda_n}\right)(1-\cos\lambda_n)\right.$$

$$\left.+\,\frac{1}{(1+A)^2}\left(\frac{\lambda_n}{\gamma_m}\right)(1-\cos\gamma_m)\right] \tag{10}$$

where the denominator Δ has been defined as

$$\Delta = \sum_{n=1}^{\infty}\sum_{m=1}^{\infty}\frac{(1-\cos\gamma_m)^2(1-\cos\lambda_n)^2}{\gamma_m^2\lambda_n^2}$$

$$\times\left[\left(1 - \frac{1}{\beta_{n,m}}\right)e^{\left(1-\sqrt{1+4\beta_{n,m}/Pe^2}\right)XPe^2/2} + \frac{1}{\beta_{n,m}}\right] \tag{11}$$

The infinite-series expansion terms in the local temperature, local mean temperature, and local perimeter-averaged Nusselt number were evaluated numerically. Care was taken to verify convergence of the infinite-series expansions for the given range of parameters (Pe, θ_e, X, etc.) studied. For small values of X, convergence of the series required a significant number of terms, whereas farther downstream convergence was rapid. To ensure that criteria for convergence was met for all cases, at least 1000 terms were required in the series summations for the cases considered here.

Results and Discussion

The dimensionless local mean temperature (θ_m) and its variation with dimensionless streamwise coordinate X are illustrated in Fig. 2 for $Pe = 5$. Data are shown for both positive and negative values of the dimensionless inlet temperature θ_e and for three channel aspect ratios, the square duct ($A = 1$) and the parallel-plate channel ($A \to 0$) being the limiting extremes. Recall that the entrance temperature is greater than the tube wall temperature for $\theta_e > 0$ and the converse is true for $\theta_e < 0$. Figure 2 reveals that the local fluid mean temperature falls or rises from its inlet value with increasing streamwise coordinate X to a positive, asymptotic, fully developed value, which is dependent only on channel aspect ratio A. The mean temperature decreases monotonically when θ_e is larger than some positive magnitude that depends on channel aspect ratio, whereas

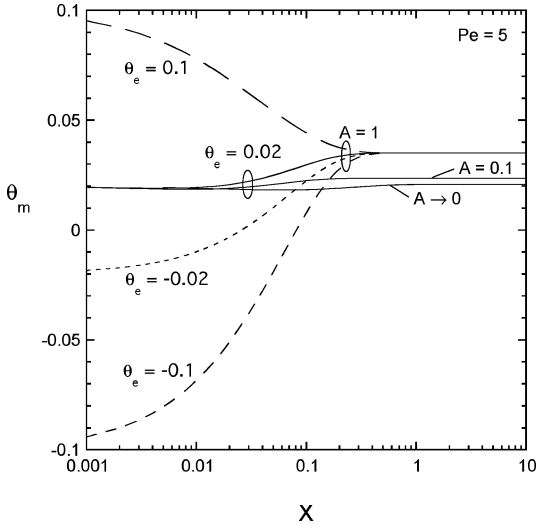

Fig. 2 Variation of local mixed mean temperature θ_m with axial position X.

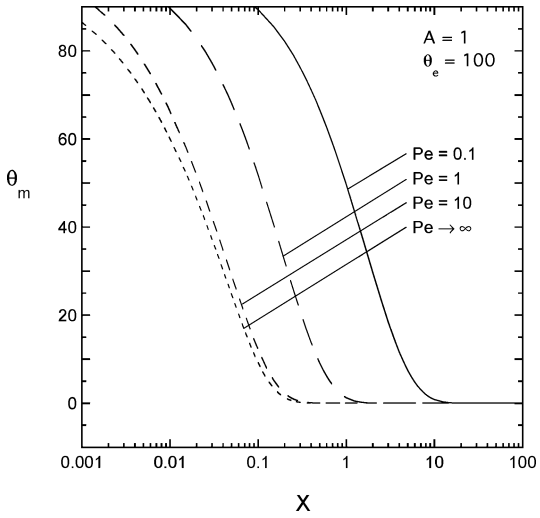

Fig. 3 Variation of local mixed mean temperature θ_m with axial position X and Peclet number.

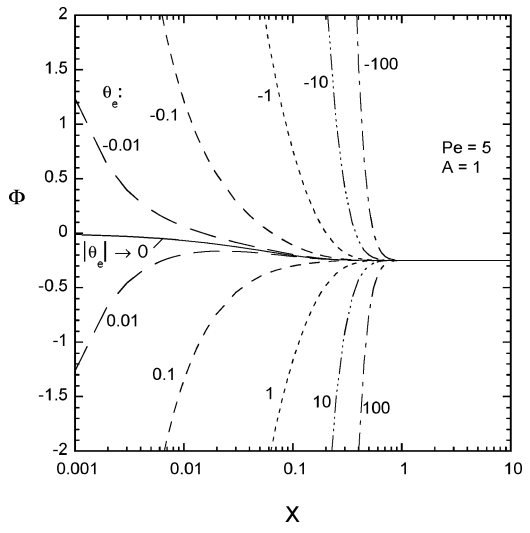

Fig. 4 Variation of the dimensionless local perimeter-averaged heat flux with axial position for both positive and negative values of the inlet temperature θ_e.

for θ_e less than this magnitude the mean temperature decreases moderately to a slight local minimum in X before increasing to its fully developed value. This local minimum may be observed for the parallel-plate channel ($A \to 0$) in Fig. 2, and this phenomenon will be explored in depth. The fully developed dimensionless fluid mean temperature decreases for increasingly slender channels, the parallel-plate channel yielding the minimum value. For all channel aspect ratios and dimensionless inlet temperatures, the mean temperature reaches its fully developed value at a dimensionless streamwise coordinate X between 0.1 and 1. The thermal development length for transport in electroosmotically induced flows is therefore significantly greater than in classical pressure-driven flow. The thermal entry length will be explored in more quantitative detail.

Figure 3 illustrates the streamwise development of the dimensionless mean temperature and its dependence on the Peclet number for a square microchannel ($A = 1$) and $\theta_e = 100$. This magnitude of dimensionless inlet temperature is representative of what would be observed for electroosmotic flow with distilled water ($\sigma \approx 10^4\ \Omega$ m, $k \approx 0.6$W/m K), a specified axial potential gradient of 150,000 V/m, a channel hydraulic diameter $D_h = 200\ \mu$m, and a temperature difference $T_e - T_w \approx 20^\circ$C. As might be expected, the thermal development occurs more rapidly for higher Pe; thermally fully developed flow occurs at smaller X for increasing Pe. Although unrealistic for electroosmotic flows, the $Pe \to \infty$ limiting case included in the figure illustrates that for sufficiently high Peclet number the normalized streamwise thermal development in X becomes independent of Pe. For this scenario the axial conduction term in the energy equation, Eq. (3), ceases to be important. For the slow-moving flows induced in electroosmotic convection, Fig. 3 reveals that both advection and diffusion terms are important and must be retained.

The dimensionless, perimeter-averaged wall heat flux at a given streamwise location is found by integrating the local wall heat flux over the duct perimeter P, as

$$\Phi = \frac{1}{P} \int_P \frac{q''_w}{i_e^2 \sigma D_h}\, \mathrm{d}P \tag{12}$$

The variation of Φ with X is shown in Fig. 4 for a square microchannel ($A = 1$) at Peclet number $Pe = 5$ for a range of positive and negative values of θ_e. For negative values of θ_e the fluid enters the channel at a temperature below that of the wall, and consequently, the heat flux early in the channel is positive (fluid heating). Conversely, for positive θ_e the opposite is true, and fluid cooling occurs. At large X, the dimensionless heat flux is negative (indicating fluid cooling) regardless of the sign or magnitude of θ_e and reaches an asymptotic value which, for a fixed channel aspect ratio, is independent of all parameters. Far downstream all volumetric heating is dissipated convectively at the wall, resulting in fluid cooling and

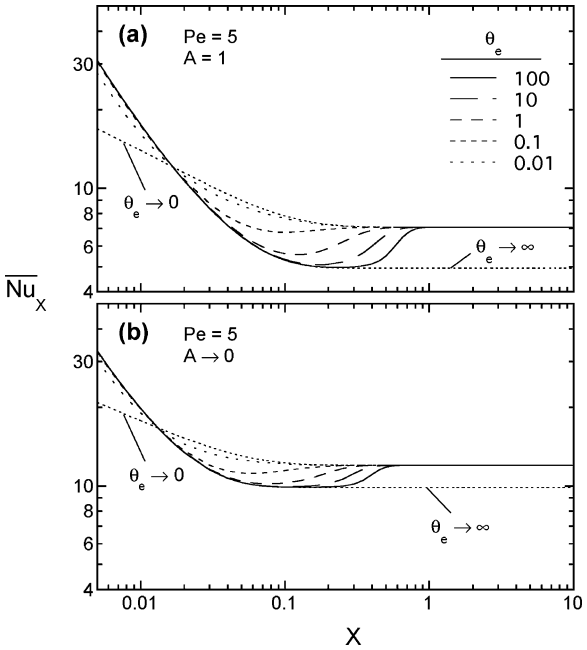

Fig. 5 Local perimeter-averaged Nusselt number as a function of X for positive values of the inlet temperature: a) square channel, $A = 1$, and b) parallel-plate channel, $A = 0$.

associated negative heat flux, mandating $\Phi = -\frac{1}{4}$. As is evident, the streamwise location where the asymptotic value is reached increases with increasing magnitude of θ_e. Thus, fluid that enters the channel at a temperature below that of the wall experiences a transition from a region of fluid heating to one of fluid cooling, passing through a point of zero wall heat flux. Thus, there also exists a unique axial location where the fluid mean temperature is identical to the wall temperature, yielding a singularity in the classical definition of the heat-transfer coefficient at this point.

An expression for the local, perimeter-averaged Nusselt number was given in Eq. (10). It may also be expressed in terms of the local perimeter-averaged wall flux and fluid mean temperature as $\overline{Nu}_X = -\Phi/\theta_m$. Figure 5 illustrates the local, perimeter-averaged Nusselt number as a function of X for positive θ_e and $Pe = 5$ for the limiting aspect-ratio cases: (a) square duct and (b) parallel-plate channel. The thermal development is illustrated for values of θ_e ranging from 0.01 to 100. Figure 5 reveals two limiting conditions corresponding to $\theta_e = 0$ and $\theta_e \to \infty$. For the $\theta_e \to \infty$ case, the local

Nusselt number is identical to the classical behavior for plug flow in a rectangular duct with constant wall temperature and no volumetric heating, for which the fully developed Nusselt numbers are 4.94 and 9.87 for $A = 1$ and 0, respectively.[29] For $\theta_e = 0$, the thermal development is dominated by volumetric generation, which must be dissipated convectively at the wall. The thermal transport for this case therefore approaches that of a constant-heat-flux boundary condition as $X \to \infty$ (indicated by $\Phi = \text{constant} = -\frac{1}{4}$ for large X in Fig. 4). The asymptotic value of the local, perimeter-averaged Nusselt numbers for the square duct and parallel-plate channel for $\theta_e = 0$ are, respectively, 7.09 and 11.98, which are considerably higher than the corresponding fully developed Nusselt number for pressure-driven duct flow without volumetric heating, $Nu_{\text{fd}} = 2.98$ and 7.54 for $A = 1$ and 0, respectively.[31] For intermediate values of θ_e, the local Nusselt numbers for both channel aspect ratios exhibit a transition between the two limiting cases. The local Nusselt number follows the $\theta_e \to \infty$ behavior at small X, merging with the $\theta_e = 0$ limiting case at large X, with a local minimum in the $\overline{Nu}_X$ versus X profile for values of $\theta_e \gtrsim 0.05$. As θ_e decreases, the point of local minimum $\overline{Nu}_X$ moves upstream, as does the point of departure from the $\theta_e \to \infty$ solution. This occurs due to the increasingly dominant contribution of Joule heating in the fluid. Figure 5 also reveals that the local perimeter-averaged Nusselt number increases with decreasing channel aspect ratio, consistent with the trend for classical laminar pressure-driven flow in rectangular channels.[29] Further, the difference in $\overline{Nu}_X$ between the $\theta_e \to \infty$ and $\theta_e = 0$ limiting cases is diminished for more slender channels.

The local perimeter-averaged Nusselt number is shown for $Pe = 5$ and $A = 1$ and 0 in Figs. 6a and 6b, respectively, for negative values of the dimensionless inlet temperature. Recall that such negative values of θ_e arise if the fluid entrance temperature is below the wall temperature. This was observed in the local heat-flux behavior of Fig. 4. In this case the fluid is heated both by Joule heating and by wall convection early in the duct (fluid-heating region), where the mean temperature is below the wall temperature. As seen in Fig. 6, the fluid-heating region is characterized by a decreasing local Nusselt number, wherein $\overline{Nu}_X$ follows that of the $\theta_e \to \infty$ limiting case. At some unique axial location the mean temperature and the wall temperature are identical, and the local Nusselt number (as traditionally defined) drops dramatically. Downstream from this location, the wall heat flux reverses direction ($\Phi < 0$, as seen in Fig. 4), the internally heated fluid is subsequently cooled convectively by the walls, and the local Nusselt number falls from an infinitely high value characteristic of the formation of a new thermal boundary layer. Ultimately, $\overline{Nu}_X$ approaches the fully developed value, merging with the $\theta_e = 0$ profile, corresponding again to the constant-wall-heat-flux condition. As the negative values of θ_e approach zero (e.g., Joule heating increases), the location of the wall heat flux reversal moves upstream. In the limiting case of $\theta_e = 0$, the heat transfer reversal occurs at an infinitesimally small X location, with no apparent singularity in the local Nusselt-number behavior. As expected for flows dominated by volumetric heating, regardless of inlet temperature, the local Nusselt number versus X profiles for both positive and negative values of θ_e (Figs. 5 and 6) become identical as $|\theta_e| \to 0$.

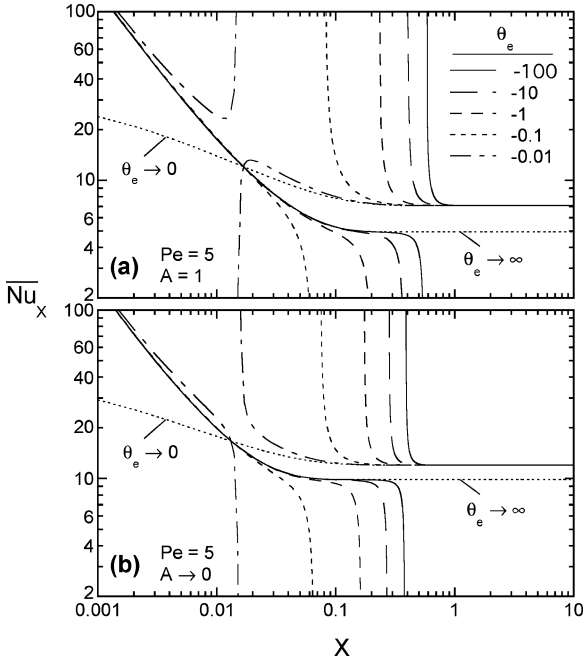

Fig. 6 Local perimeter-averaged Nusselt number as a function of X for negative values of the inlet temperature: a) square channel, $A = 1$, and b) parallel-plate channel, $A = 0$.

The local convective wall-heat flux along the perimeter of the channel at a given axial location may be illustrated by determining the Nusselt number along the side (Nu_ζ) and top/bottom (Nu_η) walls of the rectangular duct. These are found by differentiation of the local temperature profiles at the appropriate wall:

$$Nu_\zeta = \pm \frac{1}{\theta_m} \left(\frac{2A}{1+A} \right) \left. \frac{\partial \theta}{\partial \eta} \right|_{\eta = 0,1} \tag{13}$$

$$Nu_\eta = \pm \frac{1}{\theta_m} \left(\frac{2}{1+A} \right) \left. \frac{\partial \theta}{\partial \zeta} \right|_{\zeta = 0,1} \tag{14}$$

The sign is chosen specific to each wall. The variation in the local Nusselt number along the top/bottom walls, Nu_η, as a function of the lateral coordinate η for $Pe = 5$ and $\theta_e = 100$ is illustrated in Fig. 7 for $A = 0$ and 1 at four axial locations corresponding to points upstream of, at, and downstream of the Nusselt number local minimum observed in Fig. 5. Local-Nusselt-number behavior for both channel aspect ratios in Fig. 7 illustrate this minimum, where Nu_η at $X = 0.1$ lies below the $X = 0.01$ and $X = 1$ curves. It is also noted that the Nusselt number is higher at all axial locations for the parallel plate channel than for the square duct. The difference in Nu_η between the two channel aspect ratios increases with increasing X, reaching 25% at $X = 1$. It is further noted that the local Nusselt number vanishes in the corners of the channel.

Figure 8 shows the variation in local Nusselt number along both vertical and horizontal duct walls for the case of $Pe = 5$ and $\theta_e = 100$ for a slender but finite aspect ratio duct, $A = 0.1$, at the same axial locations illustrated in Fig. 7. It is noted that the local Nusselt number along the duct sidewall, Nu_ζ, is lower than its counterpart on the channel top/bottom wall, Nu_η. Again, this is more pronounced at increasing streamwise distances. Further, the local Nusselt number is approximately constant over the majority of the top and bottom surfaces for this channel aspect ratio, as seen in Fig. 8a. By

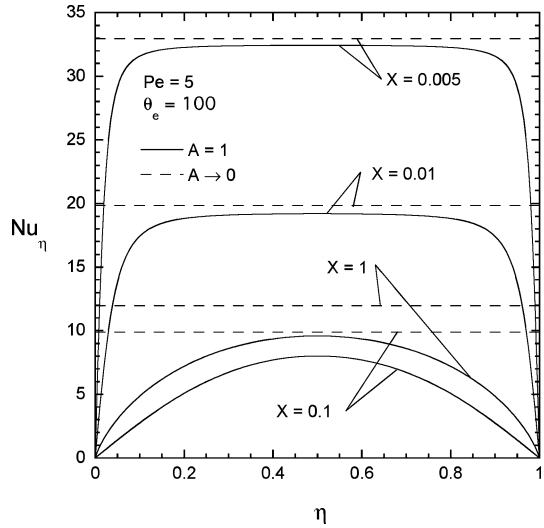

Fig. 7 Variation in local top/bottom-wall Nusselt number, Nu_η, as a function of η at four axial locations.

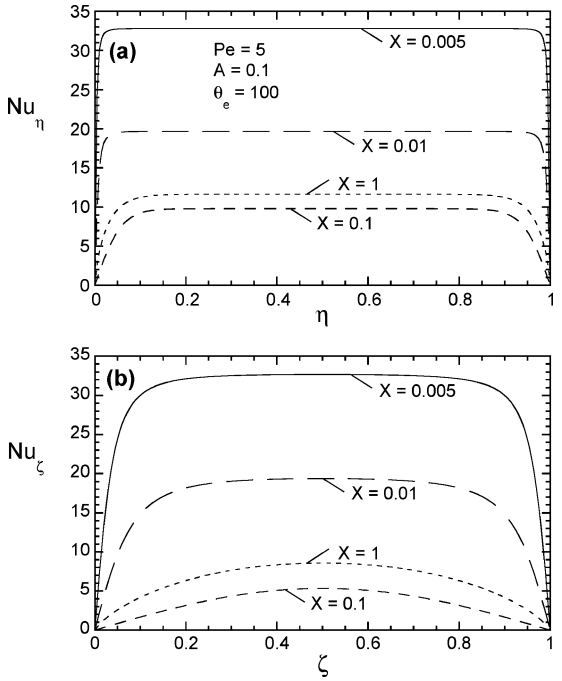

Fig. 8 Variation in the local Nusselt number along the vertical walls (Nu_ζ) and the horizontal walls (Nu_η) at four axial locations.

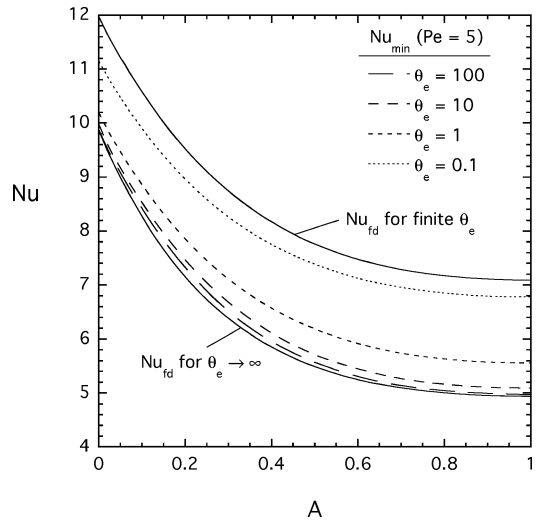

Fig. 9 Dependence of the fully developed Nusselt number on aspect ratio for the limiting cases of finite θ_e and $\theta_e \to \infty$. Also shown is the variation in $Nu_{\min}$ on A for four inlet temperatures.

contrast, there is significant variation in Nu_ζ over the sidewall surface (Fig. 8b).

The magnitude of the thermally fully developed Nusselt number (Nu_{fd}) is plotted as a function of aspect ratio in Fig. 9. Recall that for fully developed conditions, the Nusselt number is independent of both Pe and θ_e (for finite values of θ_e). The fully developed Nusselt numbers for $\theta_e \to \infty$ and for finite θ_e both exhibit decreasing magnitude with increasing channel aspect ratio. This decrease is quite significant, with the fully developed Nusselt number for the parallel-plate channel ($A = 0$) being approximately twice that for the square duct ($A = 1$). The $\theta_e \to \infty$ data reproduce the results previously published for plug-flow convective heat transfer in the absence of Joule heating.[29] Also illustrated in Fig. 9 is the aspect-ratio dependence of the minimum Nusselt number observed in the local, perimeter-averaged Nusselt-number data of Fig. 5. Recall that this minimum Nusselt number is the value reached as the thermal-transport transitions from constant-wall-temperature behavior with

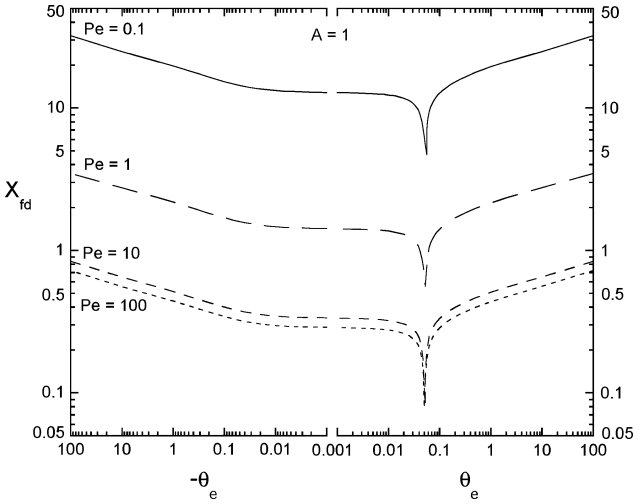

Fig. 10 Variation in thermal entry length X_{fd} with θ_e for four values of Pe.

negligible volumetric heating to that dominated by volumetric heating with resulting constant-wall-heat-flux conditions. Note that the minimum Nusselt number, which is a function of θ_e, lies between the magnitudes for the limiting cases of finite θ_e and $\theta_e \to \infty$.

The solution for the thermally developing Nusselt number and its asymptotic condition allows characterization of the thermal entry length for electroosmotically driven flow under conditions of vanishingly thin Debye layer. The entrance length X_{fd} is defined here as the X-location where the local, perimeter-averaged Nusselt number is within 0.1% of its fully developed value Nu_{fd} for a particular channel aspect ratio and Peclet number. As was seen in Fig. 5, for positive values of θ_e the local Nusselt number passes through Nu_{fd} on its way to a local minimum for $\theta_e \gtrsim 0.05$ before reaching its fully developed asymptote. Therefore, care was taken to determine the development length from the true asymptotic value. Figure 10 shows the thermal development length X_{fd} thus determined for the square channel as a function of θ_e for Pe in the range 0.1 to 100. Note that the figure abscissa is split, with negative values of θ_e shown on the left and positive values on the right. The figure reveals that X_{fd} decreases with increasing Peclet number for all values of θ_e, eventually becoming independent of Pe. In this large Peclet number limit, the thermal entry length for $|\theta_e| \to 0$ is $X_{\mathrm{fd}} \approx 0.29$. By contrast, classical pressure-driven flow in a square duct yields $X_{\mathrm{fd}} \approx 0.041$ (see Ref. 29). At low Peclet number the thermal development length is approximately $x_{\mathrm{fd}}/D_h (= X_{\mathrm{fd}} Pe) \approx 1.28$ for vanishing dimensionless entrance temperature θ_e. Thus, for $A = 1$ at low Peclet number, the thermal entry region for electroosmotic flow is approximately 7–30 times longer than that for classical pressure-driven flow. Increases in the thermal entry length of similar magnitude were noted for other channel aspect ratios. By way of illustrative example, consider the case of electroosmotically generated flow of distilled water in a fused-silica channel of square cross section of sidelength 200 μm. For an imposed potential gradient of 150 kV/m and $T_e - T_w \approx 20^\circ$C, $\theta_e \approx 100$ and $Pe \approx 16$. This scenario yields a thermal development length of approximately 2.6 mm. The development length is shorter for smaller channels.

As $|\theta_e| \to \infty$ (for both positive and negative values of θ_e), Fig. 10 reveals that the thermal development length increases in an unbounded manner. This behavior may be explained as follows. For large negative inlet temperature the Joule heating is so small as to require significant channel length before the reversal between fluid heating and fluid cooling occurs, as explained relative to Fig. 6. For large positive θ_e, the volumetric heating is so small as to require significant channel length before the departure from constant-wall-temperature ($\theta_e \to \infty$) behavior to fully developed constant-heat-flux ($\theta_e \to 0$) behavior, as seen in Fig. 5. Of course, in the limiting case of $\theta_e \to \infty$, the thermal entrance length is finite, as given by the classical problem with no volumetric heating, and is considerably smaller than for the finite-fluid Joule-heating condition.

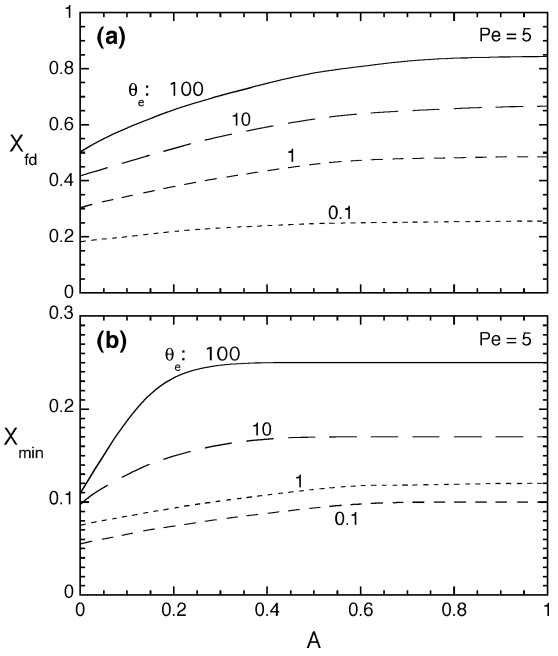

Fig. 11 Dependence of a) X_{fd} and b) X_{min} on aspect ratio for four different inlet temperatures.

There is an interesting critical point in the thermal-entry-length dependence on θ_e shown in Fig. 10 near $\theta_e \approx 0.05$. The magnitude of dimensionless inlet temperature corresponding to this critical point is actually a weak function of Pe, ranging from $\theta_e \approx 0.056$ for $Pe \to 0$ to $\theta_e \approx 0.05$ as $Pe \to \infty$. At the value of θ_e corresponding to this critical point, the local Nusselt number distribution ceases to fall below the fully developed value to a local minimum, as seen in Fig. 5a. For this nominal value of θ_e, the influence of the wall convection and the volumetric generation on the overall transport is of the same order of magnitude, and the development length is a minimum (for a given Peclet number). Despite this significant decrease in X_{fd} for $\theta_e \approx 0.05$, the thermal entry length is still considerably longer than that for pressure-driven-flow convection heat transfer.

Figures 11a and 11b illustrate, respectively, the dependence of the thermal entry length X_{fd} and the dimensionless location of the minimum Nusselt number X_{min}, on aspect ratio for $Pe = 5$ at four values of dimensionless entrance temperature. As seen in Fig. 11a, the thermal development length is a minimum for the parallel-plate channel ($A = 0$) and increases with increasing channel aspect ratio. The development length exhibits a stronger dependence on A for increasing θ_e. The thermal development for the square channel is approximately 70% longer than that for the parallel plate channel for $\theta_e = 100$. Figure 11b reveals that the axial location of the minimum Nusselt number also increases with increasing channel aspect ratio. The increase in the case of X_{min}, however, appears to be more abrupt than for X_{fd}.

Conclusions

Thermally developing, electroosmotically generated flow has been analyzed for a rectangular microchannel in the limit of vanishingly thin Debye layer under constant-wall-temperature boundary conditions. Hydrodynamically, this flow is characterized by a plug-flow velocity profile established by an imposed potential gradient along the length of the tube. The voltage gradient results in Joule heating in the fluid, with an associated volumetric source of energy. The analytical solution for the fluid-temperature development has been determined for these conditions. The solution reveals an interesting fluid mean-temperature distribution with axial position along the tube, and a local minimum in the streamwise variation in local, perimeter-averaged Nusselt number for moderate positive dimensionless tube-inlet temperature. For negative inlet temperature, which arises if the tube-entrance temperature is below the wall temperature, the fluid is initially heated, then cooled, resulting in a singularity in local Nusselt number at the heating/cooling transition location. The thermal development length is considerably larger than for traditional pressure-driven flow/heat transfer and is dependent on Peclet number and inlet temperature.

References

[1]Reuss, F. F., "Charge-Induced Flow," *Proceedings of the Imperial Society of Naturalists of Moscow*, Vol. 3, 1809, pp. 327–344.

[2]Shulin, Z., "Fabrication and Characterization of Electrokinetic Micro-Pumps," *Thermo-Mechanical Phenomena in Electronic Systems—Proceedings of the Intersociety Conference*, Vol. 2, Inst. of Electrical and Electronics Engineers, Piscataway, NJ, 2000, pp. 31–36.

[3]Culbertson, C. T., Ramsey, R. S., and Ramsey, J. M., "Electro-Osmotically Induced Hydraulic Pumping on Microchips: Differential Ion Transport," *Analytical Chemistry*, Vol. 72, No. 16, 2000, pp. 2285–2291.

[4]Dasgupta, P. K., and Shaorong, L., "Electroosmosis: A Reliable Fluid Propulsion System for Flow Injection Analysis," *Analytical Chemistry*, Vol. 66, No. 11, 1994, pp. 1792–1798.

[5]Polson, N. A., and Hayes, M. A., "Electro-Osmotic Flow Control of Fluids on a Capillary Electrophoresis Microdevice Using an Applied External Voltage," *Analytical Chemistry*, Vol. 72, No. 5, 2000, pp. 1088–1092.

[6]Arulanandam, S., and Li, D., "Liquid Transport in Rectangular Microchannels by Electro-Osmotic Pumping," *Colloids and Surfaces A*, Vol. 161, No. 1, 2000, pp. 89–102.

[7]Bousse, L., Cohen, C., Nikiforov, T., Chow, A., Kopf-Sill, A. R., Dubrow, R., and Parce, J. W., "Electrokinetically Controlled Microfluidic Analysis Systems," *Annual Review of Biophysics and Biomolecular Structure*, Vol. 29, 2000, pp. 155–181.

[8]Probstein, R. F., *Physicochemical Hydrodynamics*, 2nd ed., Wiley, New York, 1994.

[9]Valko, T. E., Siren, H., and Riekkola, M., "Characteristics of Electro-Osmotic Flow in Capillary Electrophoresis in Water and in Organic Solvents without Added Ionic Species," *Journal of Microcolumn Separations*, Vol. 11, No. 3, 1999, pp. 199–208.

[10]Burgreen, D., and Nakache, F. R., "Electrokinetic Flow in Ultrafine Capillary Slits," *Journal of Physical Chemistry*, Vol. 68, No. 5, 1964, pp. 1084–1091.

[11]Levine, S., Marriott, J. R., Neale, G., and Epstein, N., "Theory of Electrokinetic Flow in Fine Cylindrical Capillaries at High Zeta-Potentials," *Journal of Colloid and Interface Science*, Vol. 52, No. 1, 1974, pp. 136–149.

[12]Maynes, D., and Webb, B. W., "The Effect of Viscous Dissipation in Thermally Fully-Developed Electro-Osmotic Heat Transfer in Microchannels," *International Journal of Heat and Mass*, Vol. 47, No. 5, 2004, pp. 987–999.

[13]Rice, C. L., and Whitehead, R., "Electrokinetic Flow in a Narrow Cylindrical Capillary," *The Journal of Physical Chemistry*, Vol. 69, No. 11, 1965, pp. 4017–4024.

[14]Paul, P. H., Garguilo, M. G., and Rakestraw, D. J., "Imaging of Pressure and Electrokinetically Driven Flows through Open Capillaries," *Analytical Chemistry*, Vol. 70, No. 13, 1998, pp. 2459–2467.

[15]Taylor, J. A., and Yeung, E. S., "Imaging of Hydrodynamic and Electrokinetic Flow Profiles in Capillaries," *Analytical Chemistry*, Vol. 65, No. 20, 1993, pp. 2928–2932.

[16]Ross, D., Johnson, T. J., and Locascio, L. E., "Imaging of Electro-Osmotic Flow in Plastic Microchannels," *Analytical Chemistry*, Vol. 73, No. 11, 2001, 2509–2515.

[17]Tsuda, T., and Ikedo, M., "Observation of Flow Profiles in Electroosmosis in a Rectangular Capillary," *Journal of Chromatography*, Vol. 632, Nos. 1–2, 1993, pp. 201–207.

[18]Cummings, E. B., "PIV Measurement of Electro-Osmotic and Pressure-driven Flow Components in Microfluidic Systems," *Microelectromechanical Systems (MEMS)*, MEMS, American Society of Mechanical Engineers, Vol. 1, New York, 1999, pp. 377–382.

[19]Mala, G. M., Li, D., and Dale, J. D., "Heat Transfer and Fluid Flow in Microchannels," *International Journal of Heat and Mass Transfer*, Vol. 40, No. 13, 1997, pp. 3079–3088.

[20]Yang, C., and Li, D., "Analysis of Electrokinetic Effects on the Liquid Flow in Rectangular Microchannels," *Colloids and Surfaces A*, Vol. 143, Nos. 2–3, 1998, pp. 339–353.

[21]Yang, C., Li, D., and Masliyah, J. H., "Modeling Forced Liquid Convection in Rectangular Microchannels with Electrokinetic Effects," *International Journal of Heat and Mass Transfer*, Vol. 41, No. 24, 1998, pp. 4229–4249.

[22]Gobie, W. A., and Ivory, C. F., "Thermal Model of Capillary Electrophoresis and a Method for Counteracting Thermal Band Broadening," *Journal of Chromatography*, Vol. 516, No. 1, 1990, pp. 191–210.

[23]Knox, J. H., "Thermal Effects and Band Spreading in Capillary Electro-Separation," *Chromatographia*, Vol. 26, 1988, pp. 329–337.

[24]Bosse, M. A., and Arce, P., "Role of Joule Heating in Dispersive Mixing Effects in Electrophoretic Cells: Convective–Diffusive Transport Aspects," *Electrophoresis*, Vol. 21, No. 5, 2000, pp. 1026–1033.

[25]Tao, L. N., "The Second Fundamental Problem in Heat Transfer of Laminar Forced Convection," *Journal of Applied Mechanics*, Vol. 29, 1962, pp. 415–420.

[26]Tao, L. N., "On Some Laminar Forced-Convection Problems," *Journal of Heat Transfer*, Vol. 83, 1961, pp. 466–472.

[27]Maynes, D., and Webb, B. W., "Fully-Developed Electro-Osmotic Heat Transfer in Microchannels," *International Journal of Heat and Mass Transfer*, Vol. 46, No. 8, 2003, pp. 1359–1369.

[28]Maynes, D., and Webb, B. W., "Fully-Developed Thermal Transport in Combined Pressure and Electro-Osmotically Driven Flow in Microchannels," *Journal of Heat Transfer*, Vol. 125, No. 5, 2003, pp. 889–895.

[29]Shah, R. K., and London, A. L., *Laminar Flow Forced Convection in Ducts*, Academic Press, New York, 1978.

[30]Özisik, M. N., *Heat Conduction*, Wiley, New York, 1980.

[31]Kays, W. M., and Crawford, M. E., *Convective Heat and Mass Transfer*, 3rd ed., McGraw–Hill, New York, 1993.